Applied Ocean Research 70 (2018) 62–75

Contents lists available at ScienceDirect

Applied Ocean Research

journal homepage: www.elsevier.com/locate/apor

# VIV trajectories of an elastically mounted sphere

Marco Negri [a], Domenica Mirauda [b,*], Stefano Malavasi [a]

[a] Department of Civil and Environmental Engineering, Politecnico di Milano, piazza Leonardo da Vinci 32, 20133 Milano, Italy
[b] School of Engineering, Basilicata University, viale dell'Ateneo Lucano 10, 85100 Potenza, Italy

ARTICLE INFO

*Article history:*
Received 6 June 2017
Received in revised form 5 October 2017
Accepted 13 November 2017
Available online 14 December 2017

*Keywords:*
Vortex-induced vibration
Sphere
Trajectory
Phase average
Reduced velocity
Experimental model

ABSTRACT

In this paper, vortex-induced vibrations (VIV) of an elastically mounted sphere with two linear degrees of freedom have been experimentally studied. The dynamic response analysis shows that, for the range of reduced velocity from 2 to 14 here investigated, the sphere exhibits similar amplitudes and frequencies compared to the tethered sphere, and Modes I and II are detected. A new application of the phase average approach allowed extrapolating the periodic trajectory pattern from the experimental trajectories. In particular, more than one dominant harmonic component is observed in the streamwise oscillation, so the sphere trajectories are significantly different from the traditional figure-of-eight shape. The main difference is that these trajectories are not self-intersecting. Based on the experimental observations, an analytical model of the trajectory is built and discussed.



## 1. Introduction

The practical relevance of vortex-induced vibrations (VIV), as a design failure problem in bluff structures (bridges, buildings, automobiles, electric power poles, telephone cables, heat-exchanger tubes, etc.), and also as a resource of renewable energy [1], continues to raise interest in the scientific research. The sphere is one of the simplest representatives of real life bluff structures, but shows almost all the physical phenomena [2]. However, so far only few investigations have been carried out to study the dynamics of the more complex, three-dimensional problems of freely oscillating spheres in steady flows, and the majority of them are focused on the tethered spheres [3–10], to name a few.

The first Authors to observe the dynamic response of tethered spheres in steady fluid flows were Williamson and Govardhan [3]. In the transverse direction, they noted a saturation amplitude close to two diameters peak-to-peak for high Reynolds numbers ($Re = 1.13 \times 10^4$), with figure-of-eight shaped trajectories. In addition, they found a distinct collapse of data by plotting the amplitudes versus the reduced velocity, $U^* = U/f_N D$, under a range of different sphere mass ratios, $m^* = m/m_d$, from 0.082 up to 0.73. Such collapse, occurred at values of $U^* = 5$–6, was verified at the classical resonance condition, where the natural frequency is approximately equal to the vortex formation frequency. Later, Jauvtis et al. [4] named the resonance condition and the saturation state as Modes I and II, respectively. They investigated higher $m^* = 80$–940 and $U^* = 0$–300 compared to those analysed by [3], discovering two new responses: a periodic one for $20 \leq U^* \leq 40$ at $m^* = 80$, named Mode III, and another, named Mode IV, characterised by intermittent bursts of large-amplitude vibrations beyond $U^* = 100$.

In 2005, Govardhan and Williamson [5] extended their previous study on heavy spheres ($m^* > 1$). They found a large-amplitude and highly periodic mode (Mode III) at distinctly higher flow velocities, where the frequency of vibration was far below the frequency of vortex shedding for a static body. Furthermore, for both light and heavy spheres, they observed that Mode I and II in the synchronisation region were separated by a transition regime, exhibiting non-periodic vibrations. They also found that the peak amplitude and the range of the synchronisation region increased with the decreasing of the mass-damping parameter, $(m^* + C_A)\zeta$.

van Hout et al. [6,7] discovered three different bifurcation regions of a heavy tethered sphere ($m^* = 7.87$) for $2.8 \leq U^* \leq 31.1$. In the first region, the sphere oscillated with low amplitudes. The second region was characterised by periodic and large amplitude transverse oscillations of half the sphere diameter and overlapped with Modes I and II described by [4] and [5]. For the third region, the sphere exhibited non-periodic vibrations in the transverse direction, comparable to Mode IV. In the same year, a numerical and experimental study by [8] found different response amplitudes of an oscillating tethered sphere for $50 \leq Re \leq 12.000$. These regimes did not have any relation with the four modes previously described,

* Corresponding author.
*E-mail addresses:* marco.negri@polimi.it (M. Negri), domenica.mirauda@unibas.it (D. Mirauda), stefano.malavasi@polimi.it (S. Malavasi).

https://doi.org/10.1016/j.apor.2017.11.006
0141-1187/

**Nomenclature**

| | |
|---|---|
| $A$ | Transverse sectional area of the channel |
| $A_D$ | Frontal area of the sphere |
| $A_y$ | Transverse amplitude of motion |
| $A_{x1}$ | Streamwise amplitude of motion (first harmonic) |
| $A_{x2}$ | Streamwise amplitude of motion (second harmonic) |
| $C_A$ | Potential added mass coefficient ($C_A = 0.5$) |
| $D$ | Sphere diameter |
| $f_N$ | Natural frequency of the sphere in water |
| $f_{vo}$ | Vortex shedding frequency (stationary sphere) |
| $f$ | Main oscillation frequency of the sphere |
| $h$ | Distance between the free surface and sphere upper surface |
| $L$ | Rod length |
| $m$ | Sphere mass |
| $m_d$ | Displaced fluid mass |
| $\zeta$ | Non-dimensional damping coefficient |
| $U$ | Mean free-stream velocity |
| $\phi_{xy1}$ | Phase angle between streamwise and transverse position (first harmonic) |
| $\phi_{xy2}$ | Phase angle between streamwise and transverse position (second harmonic) |
| $\sigma_x$ | Standard deviation of streamwise oscillation |
| $\sigma_y$ | Standard deviation of transverse oscillation |
| $T$ | Mean period of oscillation |
| $x$ | Streamwise position |
| $y$ | Crossflow position |
| $\tilde{x}$ | Phase-averaged streamwise position |
| $\tilde{y}$ | Phase-averaged transverse position |

maybe due to the use of neutrally buoyant tethered spheres instead of light and heavy spheres.

Only recently, more attention has been paid to the study of the dynamic response of elastically mounted spheres in steady fluid flows. Computationally, Behara et al. [9] analysed the vibrations of an elastically mounted sphere of $m^* = 2$ at $Re = 300$ and reduced velocity in the range of $U^* = 0$–9. They showed that for $4.8 \leq U^* \leq 9$ the sphere exhibited two distinct synchronised oscillation regimes, each associated with a distinct wake mode: the hairpin mode and the spiral mode. Later, the same Authors [10] expanded the range of reduced velocities ($U^* = 0$–13) at $Re = 300$ and the range of Reynolds numbers to $300 \leq Re \leq 1000$, fixing $U^* = 9$. In this manner, they observed that for $9 \leq U^* < 12.2$ the sphere oscillated periodically in the transverse ($y$) and lateral ($x$) directions, depicting a circular motion on the transverse plane. On the contrary, for $U^* = 12.2$, at the end point of the synchronisation region, non-stationary oscillations were observed, and the sphere moved along elliptical orbits. In the second set of simulations, they showed how the vortex shedding mode and the sphere motion were both strongly influenced by the Reynolds number.

With regard to the experimental studies, Mirauda et al. [11–15] analysed the influence of the boundary conditions, like free surface and bottom of the channel, on the movement of an elastically mounted sphere at high Reynolds numbers ($Re = 1.7 \times 10^4$–$7.0 \times 10^4$) and for a large range of reduced velocities ($U^* = 1.90$–$7.58$) in a steady fluid flow. In particular, the Authors considered a heavy sphere characterised by a value of $m^* = 1.34$ and two sets of experiments. In the first set, they investigated the body at three different relative submergences, $h^* = h/D$: sphere close to the free surface ($h^* = 0$), to the bottom ($h^* = 3.97$) and completely immersed ($h^* = 2$). For $h^* = 2$ and $h^* = 3.97$, the displacements analysis showed Mode I at $U^* = 4.74$, a value slightly lower than that found in literature, and a transition trajectory between crescent topology and figure-of-eight shape. For $h^* = 0$, instead, they noted that the distortion of free surface reduced the transverse displacements and the shape of the trajectory became of the chaotic type. In the second set of experiments, fixing the sphere near the channel bottom, the Authors varied the water level from 0 to 2 times the body diameter. This way, they observed how, for $0 < h^* \leq 0.5$, the free surface significantly reduced the transverse oscillations of the sphere at lower flow velocities, inhibiting the formation of the typical Mode II and forestalling also Mode I at $U^* < 5$. For $h^* > 0.5$, both the modes were, instead, noted.

With the present work, the Authors have expanded on their earlier studies by investigating, through a wider range of reduced velocity, the dynamic response of an elastically mounted sphere with two linear degrees of freedom. In view of this, the following set of experiments has been carried out, in which the reduced velocity varies between 1.6 and 13.6, fixing the Reynolds number at $4.5 \times 10^4$. The analysed body vibration modes and trajectories in the $XY$ plane will contribute to provide additional insights into the VIV of a sphere completely immersed in a steady fluid flow. Furthermore, the phase average, an approach already used in literature by [5] and [16] in vorticity fields with spheres VIV, has here been adopted to describe the trajectory shape of an elastically mounted sphere, which allowed identifying the "synchronised pattern" between the transverse and streamwise motion.

The outline of the paper is as follows. In Section 2, the experimental setup and the data analysis are described. The analytical modelling of the sphere trajectories are shown and discussed in Section 3. In Section 4 the dynamic response in amplitude and frequency of the sphere and the trajectory shapes on the $XY$ plane are analysed. Finally, the main findings of the present work are summarised in Section 5.

## 2. Experimental setup and data treatment

Experiments were performed in an open water channel at the Hydraulics Laboratory of the Politecnico di Milano, with a cross section of $50 \times 60$ cm and a 6 m length. The experimental model was a sphere made of PVC plastic, covered in paint in order to reduce the surface roughness. The diameter was $D = 90 \pm 0.02$ mm and the mass ratio was $m^* = 1.24 \pm 0.01$. The sphere was connected through a threaded coupling to one end of a stainless steel rod of circular section with a diameter of $3 \pm 0.02$ mm. The other end of the rod was clamped to a fixed aluminium structure mounted on the channel and located above it. The type of restraint allowed the sphere to move mostly in the $XY$ plane, while the displacements along the vertical direction, $Z$, were negligible. In Fig. 1 a scheme of the experimental apparatus is shown.

The spherical body was completely immersed ($h/D = 2$) in a free surface flow with water depth equal to 5 times the sphere diameter, while the blockage coefficient ($\gamma_b = A/A_D$) was constant, and equal to 0.03.

The sphere movements were recorded through a CCD (Charge Coupling Device) with an acquisition frequency of 50 Hz and a resolution of $659 \times 493$ px. The camera was located below the water channel. The sphere had a fluorescent circular marker at its bottom (aligned with its centre of gravity), which allowed acquiring well-contrasted images in the darkness, with the bright marker on a black background. Therefore, the image processing necessary to calculate the position of the marker was quite simple, and consisted in converting each frame into a binary image imposing a threshold brightness, and then calculating the centroid of the blob associated to the marker. Taking into account the spatial resolution of the images, 2.45 px/mm, and the average blob diameter, 9 px, the uncertainty of the marker position was 0.02 mm.

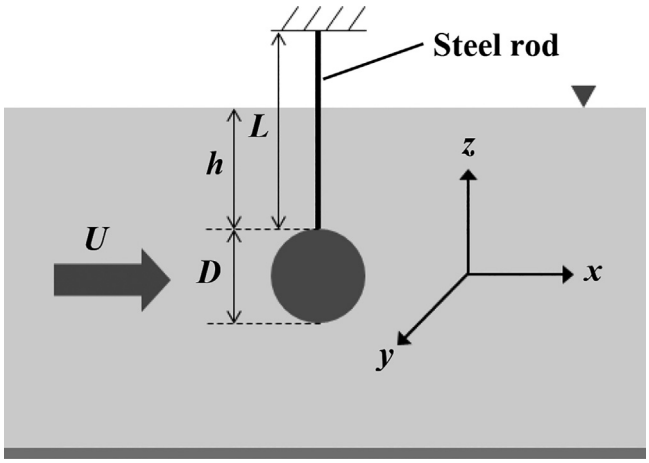


**Fig. 1.** Scheme of the experimental apparatus. The origin of the reference system is in the sphere centre.

The values of the natural frequency in water, $f_N$, were experimentally determined hypothesising the behaviour of the sphere similar to that of a linear single degree-of-freedom (SDOF) oscillator. In the case here analysed, the response of the sphere was obtained by isolating the single mode of interest, since the natural frequencies of the system were sufficiently separated everywhere. The adopted procedure was the following: a) recording through a CCD camera of several free decay oscillations of the sphere, set free to oscillate from an initial position; b) evaluation of the power spectral density (PSD) function from the recorded signal; c) identification on the PSD of the natural frequency of the first mode in water, $f_N$. The natural frequencies, $f_N$, went from 3.39 Hz to 0.41 Hz with increasing $L/D$ ratio from 2.2 to 10 (where $L$ includes half the sphere diameter).

In the tests in flowing water, the $x$ and $y$ time-coordinates of the sphere were processed by means of phase average. This was possible because, in all the cases analysed, at least one component of the sphere movement was harmonic and was used as reference phase for itself and the other motion component. For example, in Fig. 2a and b, a piece of the time history of $x$ and $y$ is reported for two experimental tests ($U^*=4.3$ and $U^*=9.6$). In the first case (Fig. 2a), the $x$-component of motion is harmonic while the $y$-component is more chaotic, vice versa in the second case (Fig. 2b). In Fig. 2c and d, the spectra of the two components of motion are shown.

The reference phase was built by low-pass filtering (cut-off frequency equal to 1.2 times the main frequency of the signal spectrum) of the periodic signal ($x$ or $y$), and then detecting its points of relative maxima, which were used as period trigger. The mean period $T$ of the signal was calculated by averaging the duration of the periods found inside the signal. Subsequently, data ($x$ and $y$) were re-sorted by assigning a new time-coordinate to each sample, which was the time-lag between the sample and the closest trigger point in the reference signal. Re-sorted data were then averaged by means of a moving average window going from $-T/2$ to $T/2$ (width of window = $T/20$); the result was a "mean oscillation cycle" of $x$ and $y$ motion. Fig. 2e–h show the phase-sorted (point) and the phase-averaged (line) data of the two experimental tests. This kind of phase average is very similar to the one explained in more detail in [17].

The mean period of the phase average was used to define the oscillation frequency of the sphere $\omega = 2\pi f = 2\pi/T$. Therefore, the dimensionless frequency was calculated as $f^* = f/f_N$.

The mean amplitude and phase of the sphere motion were calculated as Fourier coefficients of the phase-averaged quantities $\tilde{x}$ and $\tilde{y}$:

$$A_y^* = A_y/D \equiv \frac{2}{T}\left|\int_{-T/2}^{T/2} \tilde{y} e^{-i\omega t} dt\right| /D \tag{1}$$

$$A_{x,n}^* = A_{x,n}/D \equiv \frac{2}{T}\left|\int_{-T/2}^{T/2} \tilde{x} e^{-in\omega t} dt\right| /D \tag{2}$$

$$\phi_y \equiv arg\left(\int_{-T/2}^{T/2} \tilde{y}\, e^{-i\omega t} dt\right) \tag{3}$$

$$\phi_{x,n} \equiv arg\left(\int_{-T/2}^{T/2} \tilde{x} e^{-in\omega t} dt\right) \tag{4}$$

where $n = 1, 2$. In the next paragraph, the analytical representation of Eqs. (1)–(4) is explained in more details.

## 3. Trajectory analytical modelling

A discrete Fourier transform on the phase-averaged motion components $\tilde{x}$ and $\tilde{y}$ revealed that the trajectories of the sphere are always well represented by the following expressions:

$$\tilde{y}/D \cong A_y^* \sin(\omega t) \tag{5}$$

$$\tilde{x}/D \cong A_{x1}^* \sin\left(\omega t + \phi_{xy1}\right) + A_{x2}^* \sin\left(2\omega t + \phi_{xy2}\right) \tag{6}$$

where $\phi_{xy1}$, $\phi_{xy2}$ are calculated by re-arranging the phases of Eqs. (3) and (4).

The reliability of this representation is demonstrated in the appendix, where the Fourier coefficients of the phase-averaged data are calculated up to further harmonics. As a result, their increase does not effectively improve the model of the trajectory: the analysis of the Fourier coefficients and the residual between the phase average trajectory and its inverse Fourier transform reveals that the transverse motion is completely represented by one harmonic, and the streamwise motion is completely represented by a maximum of two harmonics. Therefore, the trajectories can be subdivided into two groups:

- 1:1 trajectories: first harmonic in the streamwise motion, first harmonic in the crossflow motion;
- 2:1 trajectories: second (and eventually first) harmonic in the streamwise motion, first harmonic in the crossflow motion.

It should be noted that only the integer multiples of the main harmonic $\omega$ have been considered in this model, because the operation of phase average cancels the contribution of the other frequencies, which do not determine a recurrent and recognisable pattern in the trajectory anyway. Looking at the Eqs. (5) and (6), the parameters that define the shape of a trajectory can be identified. A possible list of them can be $A_y^*/A_x^*$, $\phi_{xy1}$, for the 1:1 trajectory and $A_y^*/A_{x2}^*, A_{x1}^*/A_{x2}^*$, $\phi_{xy1}$, $\phi_{xy2}$, for the 2:1 trajectory. It is interesting to further subdivide these parameters into two groups: the ones that change only the $XY$ aspect ratio (stretching or shrinking the trajectory) and the ones that cause a more effective change of shape. The latter are $\phi_{xy1}$ for the 1:1 trajectory and $A_{x1}^*/A_{x2}^*$, $\phi_{xy1}$, $\phi_{xy2}$, for the 2:1 trajectory.

Fig. 3 reports the trajectories according to Eqs. (5) and (6), as a function of the suggested "effective" parameters. Only a quadrant of the domain $\phi_{xy1}$, $\phi_{xy2}$ is reported; it includes the experimental values found in this work, and it is also representative for many

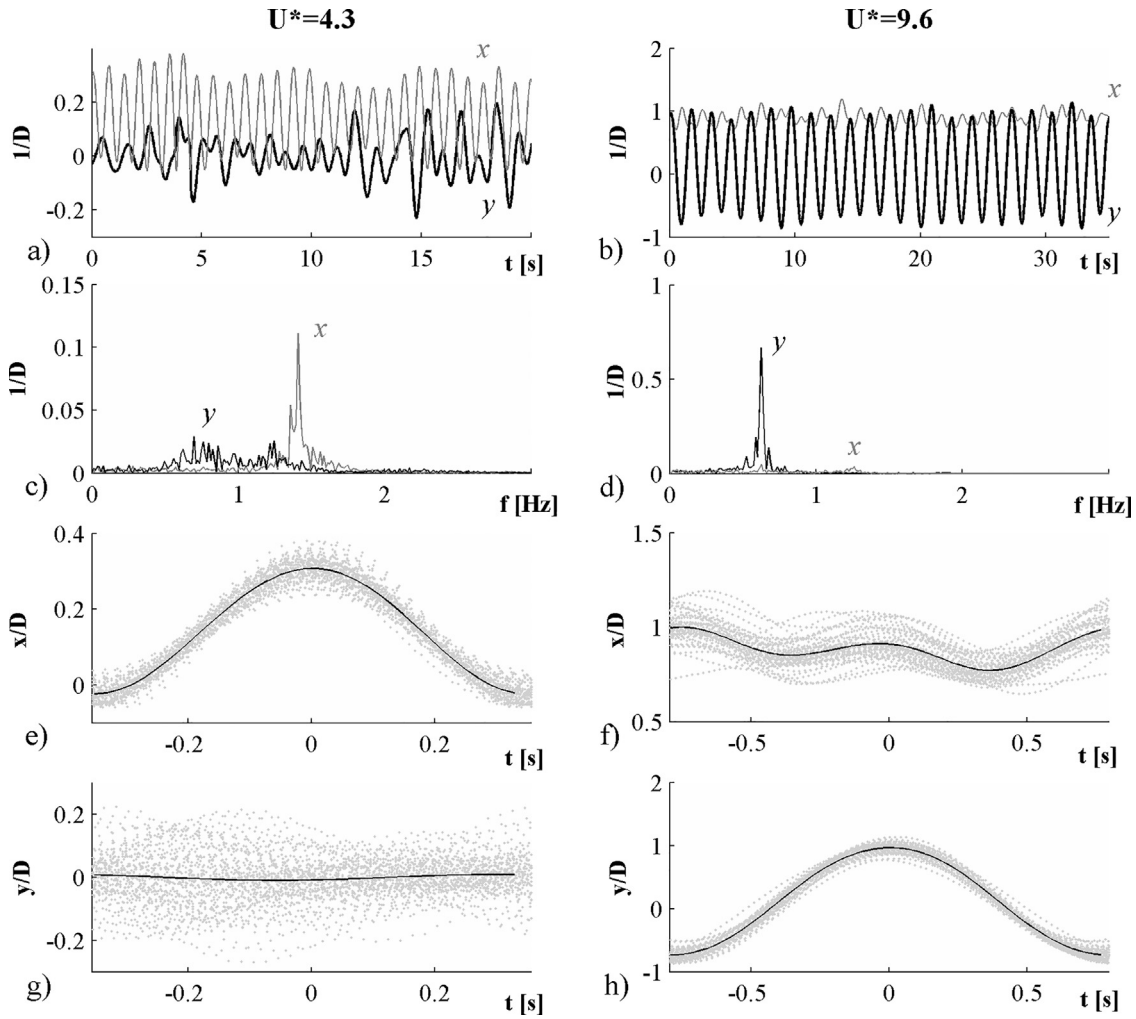


**Fig. 2.** Examples of experimental data and processing for tests $U^*=4.3$ and $U^*=9.6$. a), b) piece of $x$ and $y$ time histories; c), d) $x$ and $y$ spectra of the tests; e), f) phase-sorted (point) and phase-averaged (line) $x$-data; g), h) phase-sorted (point) and phase averaged (line) $y$-data.

trajectories of tethered spheres and elastically mounted cylinders found in VIV literature.

The trajectories in Fig. 3 are subdivided into two main groups: the 1:1 trajectories on the left hand side (red background) and the 2:1 trajectories on the right hand side (violet and blue background) of the figure. The 2:1 trajectories with blue background do have not the first harmonic in the $x$ component, so they are represented out of the $\phi_{xy1}$ domain, for simplicity purpose. The vertical axis of the figure, $\phi_{xy1}$, applies to 1:1 and 2:1 trajectories, while the horizontal axis $\phi_{xy2}$ applies only to 2:1 trajectories. In the 2:1 trajectories, the effect of the parameter $A^*_{x1}/A^*_{x2}$ is also considered. The number reported next to the trajectories is the critical value of $A^*_{x1}/A^*_{x2}$, whose meaning will be explained later. The domain of $\phi_{xy1}$ and $\phi_{xy2}$ in Fig. 3 includes half of 1:1 trajectories and a quarter of 2:1 trajectories. However, the reported analysis can be easily extended to the rest of the domain.

The effective shape of 1:1 trajectories depends only on $\phi_{xy1}$. These trajectories are an ellipse, which is reduced to a line segment when $\phi_{xy1}=0$ or $\phi_{xy1}=\pi$. In the present results, these trajectories always happen with very low $A^*_y/A^*_{x1}$, which means that the main direction of motion is the streamwise one. $\phi_{xy1}$ determines the sign of the ellipse inclination and the direction of rotation: for $-\pi/2<\phi_{xy1}<\pi$, the inclination is negative (the inclination sign is sgn(cos $\phi_{xy1}$)), while for $0<\phi_{xy1}<\pi$ the direction of rotation is counter clockwise (the rotation direction is sgn(sin $\phi_{xy1}$)).

The 2:1 trajectories are depicted as a function of $A^*_{x1}/A^*_{x2}$, $\phi_{xy2}$, $\phi_{xy1}$ ($A^*_y/A^*_{x2}$, which is the $XY$ aspect ratio, is not constant in the representations). According to the experimental results here presented and VIV literature, these trajectories always happen with high $A^*_y/A^*_{x2}$, which means that the main direction of motion is the transverse one. Four values of $A^*_{x1}/A^*_{x2}$ (0, 1, 2, 5) are considered in Fig. 3, and they are recognisable by the thickness of the line.

The first row of the 2:1 trajectories has $A^*_{x1}/A^*_{x2}=0$ and it is the "classical" 8-shaped VIV trajectory, which is a Lissajous figure. It has no dependence on $\phi_{xy1}$, and the parameter $\phi_{xy2}$ only determines the shape of the trajectory (apart from the $XY$ aspect ratio), the sign of the concavity and the direction of rotation of the trajectory. The sign of the concavity is $-$sgn(sin $\phi_{xy2}$) and, for $\pi<\phi_{xy2}<2\pi$, the trajectory concavity is positive (towards downstream). The trajectory is reduced to a chord (the crescent topology in VIV) for $\phi_{xy2}=3\pi/2$ and $\phi_{xy2}=\pi/2$. For $\pi/2<\phi_{xy2}<3\pi/2$, the direction of rotation is such that the trajectory moves downstream at the top of the figure-of-eight, named "clockwise motion" by [18]. Therefore, in that definition, the rotation direction is sgn $\left(\cos\,\phi_{xy2}\right)$.

The influence of the phase lag $\phi_{xy2}$ on the direction of rotation of 8-shaped trajectories was already highlighted in [19]. In that work, the phase lag was calculated according to the cosine phase, hence the present $\phi_{xy2}$ should be shifted by $\pi/2$ to be compared with the phase lags of [19]. The presence of the first harmonic also in the streamwise motion ($A^*_{x1}/A^*_{x2}>0$) determines trajectory shapes that are sometimes different from the classical 8-shape, especially

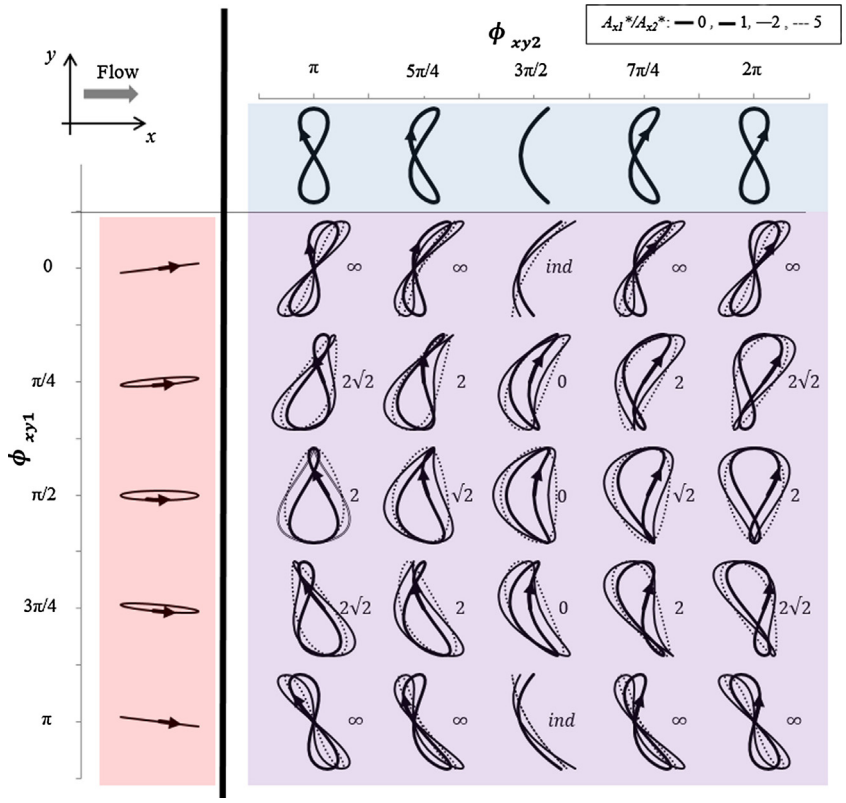


**Fig. 3.** Analytical model of VIV trajectories: the first column on the left (red background) contains 1:1 trajectories; the first row at the top (blue background) contains 2:1 trajectories with only second harmonic in the $x$ component; in the centre (violet background) there are the 2:1 trajectories with both first and second harmonic in the $x$ component. The number next to each trajectory is the critical ratio $\left(A_{x1}^*/A_{x2}^*\right)_{crit}$. (For interpretation of the references to colour in this figure legend, the reader is referred to the web version of this article.)

because they can be not self-intersecting. Such trajectories have been encountered in this study and are also visible in some previous works on cylinder VIV, in which the natural frequency of the cylinder in the $x$ and $y$ directions is different [20,21]. In those studies, besides the classical 8-shape, the authors detected other types of trajectories, which they called "D", "egg", and "rain drop" shape. These shapes are also recognisable in Fig. 3, and their occurrence is linked to the values of $A_{x1}^*/A_{x2}^*$, $\phi_{xy2}$, $\phi_{xy1}$.

The magnitude of $A_{x1}^*/A_{x2}^*$ indicates the relative importance of the first and second harmonic. If $A_{x1}^*/A_{x2}^* \to 0$, the trajectory tends to the 8-shape (including its degeneration to the crescent topology) while, if $A_{x1}^*/A_{x2}^* \to \infty$, the trajectory tends to the 1:1 trajectory shape, which is the ellipse (and its degeneration to the segment). Between these extreme cases there are some intermediate shapes.

For $\phi_{xy1} \approx 0$ and $\phi_{xy1} \approx \pi$, the trajectory is always self-intersecting (8-shape or chord when $\phi_{xy2} = 3\pi/2$) regardless of $A_{x1}^*/A_{x2}^*$. For $\phi_{xy1} \neq 0$ and $\phi_{xy1} \neq \pi$, the increase of $A_{x1}^*/A_{x2}^*$ changes dramatically the shape of the trajectory: if $\phi_{xy2} \neq 3\pi/2$, the trajectory shifts to the "rain-drop" and then to the "egg" shape while, if $\phi_{xy2} \approx 3\pi/2$ or $\phi_{xy2} \approx \pi/2$, the chord-trajectory "opens" into the "D" shape. Actually, the "rain-drop" shape is the critical passage between the "8" and the "egg" shapes, in which the self-intersecting point of the trajectory is a cusp. Therefore, the occurrence of a non-derivable point in the trajectory marks the passage from a self-intersecting trajectory (8-shape or a chord) to a non-self-intersecting trajectory ("egg" or "D"). By detecting when $dy/dx$ is undetermined, it is possible to identify this critical condition as:

$$\left(A_{x1}^*/A_{x2}^*\right)_{crit} = 2\left|\frac{\cos\phi_{xy2}}{\sin\phi_{xy1}}\right| \tag{7}$$

The trajectory is self-intersecting (8-shape or chord) when $A_{x1}^*/A_{x2}^* < \left(A_{x1}^*/A_{x2}^*\right)_{crit}$, otherwise it is not self-intersecting ("egg" or "D" shape). If $A_{x1}^*/A_{x2}^* = \left(A_{x1}^*/A_{x2}^*\right)_{crit}$, the trajectory has a cusp and can be considered as "rain-drop" shape.

This critical value is reported in Fig. 3 on the right of each trajectory. Three particular cases occur:

- $\left(A_{x1}^*/A_{x2}^*\right)_{crit} = 0$ the trajectory is self-intersecting only if $A_{x1}^*/A_{x2}^* = 0$, and in that case it is a chord.
- $\left(A_{x1}^*/A_{x2}^*\right)_{crit} = \infty$ the trajectory is always self-intersecting (8-shape or chord) regardless of$A_{x1}^*/A_{x2}^*$; if $A_{x1}^*/A_{x2}^* \to \infty$, the trajectory is a chord.
- $\left(A_{x1}^*/A_{x2}^*\right)_{crit} = ind$ (indeterminate) the trajectory is always self-intersecting (chord) regardless of $A_{x1}^*/A_{x2}^*$.

Therefore, the sharpening of the trajectory on one side is linked to $A_{x1}^*/A_{x2}^*$, $\phi_{xy1}$, $\phi_{xy2}$. The trajectory tip (or the smallest lobe of the 8) is in the region $y < 0$ if $\mathrm{sgn}(\cos\phi_{xy2})/\mathrm{sgn}(\sin\phi_{xy1}) > 0$: that means that for $3\pi/2 < \phi_{xy2} < 5\pi/2 \cap 0 < \phi_{xy1} < \pi$ and $\pi/2 < \phi_{xy2} < 3\pi/2 \cap \pi < \phi_{xy1} < 2\pi$ the downer part of the trajectory is pointed and the upper part is rounded. $A_{x1}^*/A_{x2}^*$ determines the relative dimension of the two lobes in the self-intersecting trajectories, and the amount of concavity in the not self-intersecting trajectories.

As for the classical 8-shaped trajectories, $\pi < \phi_{xy2} < 2\pi$ implies concavity towards downstream.

As for the 1:1 trajectories, $\phi_{xy1}$ determines the sign of the trajectories inclination, which is positive for $-\pi/2 < \phi_{xy1} < \pi/2$, (reference system of Fig. 3). In the trajectories that are not self-intersecting, $0 < \phi_{xy1} < \pi$ determines counter clockwise direction of rotation (in its common sense).

**Table 1**
Geometrical properties of 2:1 trajectories.

| Property | Condition/expression |
|---|---|
| Self-intersection | $A^*_{x1} = 0$ or $\frac{A^*_{x1}}{A^*_{x2}} < 2\left\lvert\frac{\cos\phi_{xy2}}{\sin\phi_{xy1}}\right\rvert$ |
| Rotation direction of self-intersecting trajectories (according to [18]) (positive if counter clockwise) | $\mathrm{sgn}(\cos\phi_{xy2})$ |
| Concavity sign (positive if concavity is towards downstream) | $-\mathrm{sgn}(\sin\phi_{xy2})$ |
| Rotation direction for not self-intersecting trajectories (also for 1:1 trajectories) (positive if counter clockwise, according to the present reference system) | $\mathrm{sgn}(\sin\phi_{xy1})$ |
| Inclination sign (also for 1:1 trajectories) (according to the present reference system) | $\mathrm{sgn}(\cos\phi_{xy1})$ |
| Position of the tip (or smallest lobe) (positive if tip is in the region $y>0$, according to the present reference system) | $-\frac{\mathrm{sgn}(\cos\phi_{xy2})}{\mathrm{sgn}(\sin\phi_{xy1})}$ |

**Table 2**
Characteristic parameters of the experiments.

| $L/D$ | $f_N$ [Hz] | $\zeta$ | $U^*$ | $Re$ |
|---|---|---|---|---|
| 2.22 | 3.39 | 0.009 | 1.6 | $4.50\times10^4$ |
| 3.89 | 1.54 | 0.012 | 3.6 | |
| 4.44 | 1.28 | 0.013 | 4.3 | |
| 4.72 | 1.18 | 0.013 | 4.7 | |
| 5.00 | 1.08 | 0.014 | 5.1 | |
| 5.28 | 1.01 | 0.014 | 5.5 | |
| 5.56 | 0.94 | 0.015 | 5.9 | |
| 6.11 | 0.82 | 0.016 | 6.8 | |
| 6.67 | 0.72 | 0.017 | 7.7 | |
| 7.22 | 0.65 | 0.018 | 8.5 | |
| 7.78 | 0.58 | 0.019 | 9.6 | |
| 8.33 | 0.53 | 0.020 | 10.5 | |
| 8.89 | 0.48 | 0.021 | 11.6 | |
| 9.44 | 0.44 | 0.021 | 12.6 | |
| 10.00 | 0.41 | 0.022 | 13.6 | |

Table 1 is a summary of the geometrical properties of the 2:1 trajectories.

## 4. Discussion of the results

The tests were carried out maintaining the mean stream velocity constant ($U = 0.5 \pm 0.001$ m/s) and changing $L/D$, in order to modify the natural frequency of the system. This allowed investigating a sufficiently wide range of reduced velocity and verifying the efficacy of the non-dimensional parameters used to study the phenomenon. Table 2 shows the characteristic parameters of the experiments. The damping ratio $\zeta$ increases with the rod length, and it is included in the range 0.009–0.022. Therefore, the mass-damping parameter $(m^* + C_A)\zeta$ is included in the range 0.016–0.038 and should slightly affect the sphere amplitude of motion.

Fig. 4 reports the variation, with the reduced velocity, $U^*$, of the normalised amplitudes ($A^*_y$, $A^*_{x1}$, $A^*_{x2}$) of oscillation in the $XY$ plane. For the streamwise motion, the value $\sqrt{2}\sigma_x/D$ is also shown, which is useful to compare the present results with the ones in literature.

It is evident that the value $U^* = 5$ divides the chart of Fig. 4 into two parts: for $U^* < 5$ the motion is mostly in the streamwise direction, while for $U^* > 5$ the transverse motion component is preponderant. Moreover, for $U^* > 5$ the streamwise component is characterised by two harmonics, whose amplitudes are comparable.

Looking at the transverse amplitude $A^*_y$, the sphere is seen to exhibit the classic amplitude response of the tethered sphere, with Modes I and II. The first one starts the lock-in regime at $U^* \approx 5$ and persists up to $U^* \approx 8$. This branch is characterised by large transverse amplitude oscillations with $0.4 \leq A^*_y \leq 0.65$. The second response amplitude branch occurs at $U^* \approx 10$ and continues up at least to the end of the present measurements $U^* \approx 14$. In this branch, the sphere starts undergoing oscillations that are higher than the amplitudes corresponding to the first response branch ($0.8 \leq A^*_y \leq 1$). The maximum transverse amplitude, $A^*_y \approx 1$, is greater than the saturation value 0.9 found by Govardhan and Williamson [5] with Reynolds number up to 12000. Taking also into account that the mass parameter $(m^* + C_A)\zeta$ is a little higher than 0.02 (the value below which it is not influential), this higher amplitude could be due to the high Reynolds number. As a matter of fact, Govardhan and Williamson [22] found that the maximum amplitude of cylinder VIV increases with the Reynolds number, at least in the range 1000–33000.

The presence of two vibration modes is furtherly confirmed by Fig. 5, where the results here analysed for a heavy sphere of $m^* = 1.24$ are compared to those obtained for light tethered spheres of $m^* = 0.45$ [5] and $m^* = 0.8$ [4] and for a heavy tethered sphere of $m^* = 2.8$ [4].

The figure shows a different behaviour in function of the mass ratio. In particular, in the case of the light tethered sphere, $m^* = 0.45$, the transition between the two modes is clearly exhibited through a jump. Besides, [5] demonstrated that the two modes are characterised by periodic transverse oscillations while, in the transition regime, the transverse oscillations are not periodic. Instead, in the case of sphere of higher mass, $m^* = 2.8$, the data do not show any clear separation but a change in concavity from Mode I to Mode II [4]. In fact, the transition between the two modes is more continuous and the response seems to remain periodic. The data here investigated, with $m^* = 1.24$, have a trend similar to that of a heavy sphere with $m^* = 2.8$ and, as shown in Fig. 6f, the transition from Mode I to Mode II does not present a change of periodicity in the time histories of the transverse oscillations.

With regard to the streamwise oscillation, it is interesting to note that $U^* = 5$ represents a significant change in motion dynamics. In fact, for $U^* < 5$ the streamwise component is made of only one harmonic ($A^*_{x1}$), while for $U^* > 5$ it is made of two harmonics ($A^*_{x1}$ and $A^*_{x2}$). Therefore, $U^* = 5$ is the transition from the 1:1 $XY$ synchronisation to the 2:1 $XY$ synchronisation. The first harmonic $A^*_{x1}$ increases up to 0.18 until $U^* \approx 5$, where it sharply decreases to zero. Subsequently, for $U^* > 5$ the second harmonic $A^*_{x2}$ also appears, and $A^*_{x1}$ and $A^*_{x2}$ increase from zero to about $0.06 \div 0.08$ in $U^* = 12$, where they reach a maximum. For $U^* > 12$, $A^*_{x1}$ and $A^*_{x2}$ slightly decrease. For $U^* > 5$, $A^*_{x1}$ and $A^*_{x2}$ are of the same magnitude order. The value of $\sqrt{2}\sigma_x/D$ for $U^* > 5$ is slightly less but comparable with the streamwise amplitudes found in Govardhan and Williamson [5] with a tethered sphere of $m^* = 0.45$.

In Fig. 7, the parameters that are linked to the trajectory shape are reported. Fig. 7a shows the phase lags $\phi_{xy1}$ and $\phi_{xy2}$ between streamwise and transverse motions, and Fig. 7b shows the ratio $A^*_{x1}/A^*_{x2}$ and its critical value, calculated as Eq. (7). It is useful to link these parameters to the experimental trajectories, which are reported in Fig. 8; there, the raw experimental trajectories, the phase-averaged experimental trajectories and the inverse Fourier transform of the latter are reported. Looking at Fig. 7a, $0 \leq \phi_{xy1} \leq \pi$ for the range of $U^*$ investigated in this work. Referring to Fig. 3, this means negative inclination of the trajectory and counter clockwise motion for the 1:1 trajectories ($U^* < 5$) and for the 2:1 trajecto-

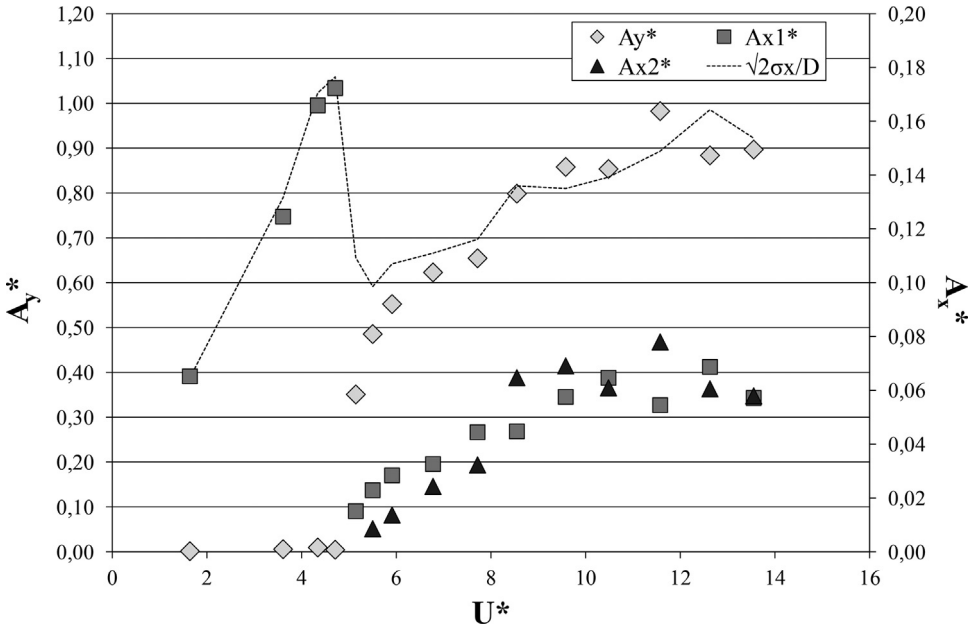


**Fig. 4.** Amplitudes of transverse and streamwise motion.

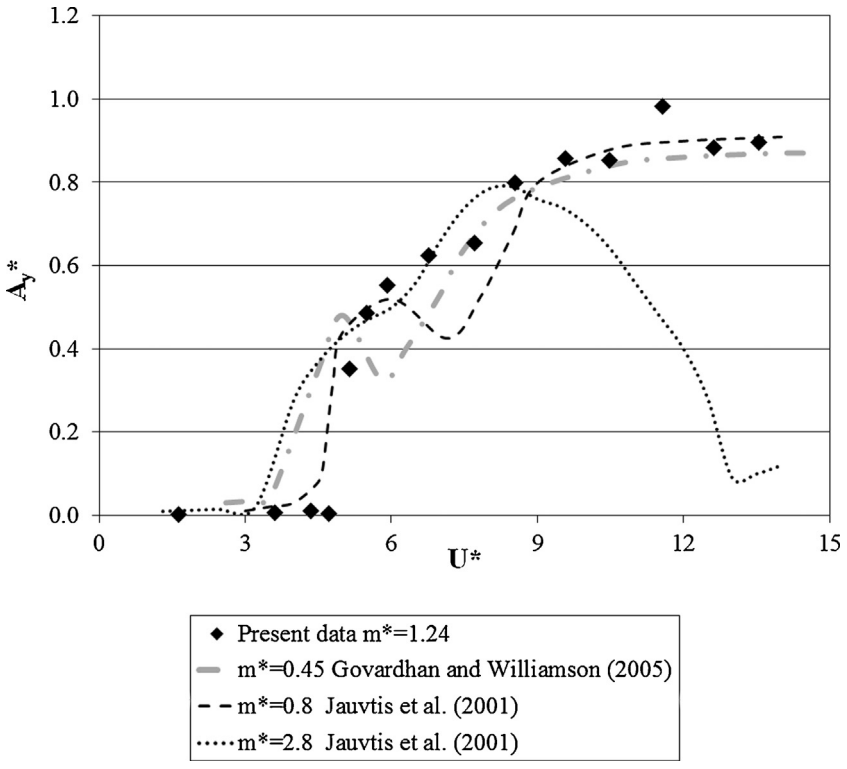


**Fig. 5.** Transverse amplitude as a function of reduced velocity. Present data and literature results.

ries ($U^* > 5$) with $A^*_{x1}/A^*_{x2} > \left(A^*_{x1}/A^*_{x2}\right)_{crit}$ (*i.e.* not self-intersecting trajectory).

$\phi_{xy1}$ is almost always included between $3\pi/4$ and $\pi$ and is slightly decreasing with $U^*$. In fact, for $U^* < 5$ the transverse amplitude motion $A_y{}^*$ is very small, so the value of $\phi_{xy1}$ is sensitive to small changes in the trajectory shape. This could explain why, in $U^* = 3.6$, $\phi_{xy1}$ quite disagrees with the neighbouring points. The value assumed by $\phi_{xy1}$ for $U^* < 5$ is close to $\pi$ or 0, so the elliptic trajectory is almost a segment. In Fig. 8, the 1:1 trajectory for $U^* = 4.3$ is represented, where the periodic component of transverse motion, visible in the phase-averaged trajectory, is very small with respect to the chaotic, unsynchronised component of streamwise motion.

For $U^* > 5$, the second harmonic appears in the streamwise component. The phase lag $\phi_{xy2}$ (Fig. 7a) increases with $U^*$ and is included in the range $\pi \leq \phi_{xy2} \leq 7\pi/4$. $\phi_{xy2}$ seems to have two plateaus, one in Mode I ($\phi_{xy2} \approx 7\pi/6$) and one in Mode II ($\phi_{xy2} \approx 5\pi/3$).

Fig. 7a also indicates that the self-intersecting trajectories are, according to the definition of [18], clockwise($\phi_{xy2} < 3\pi/2$) in Mode I and in the transition region, while they are counter clockwise ($\phi_{xy2} > 3\pi/2$) in Mode II. Fig. 8 shows that the clockwise trajectories

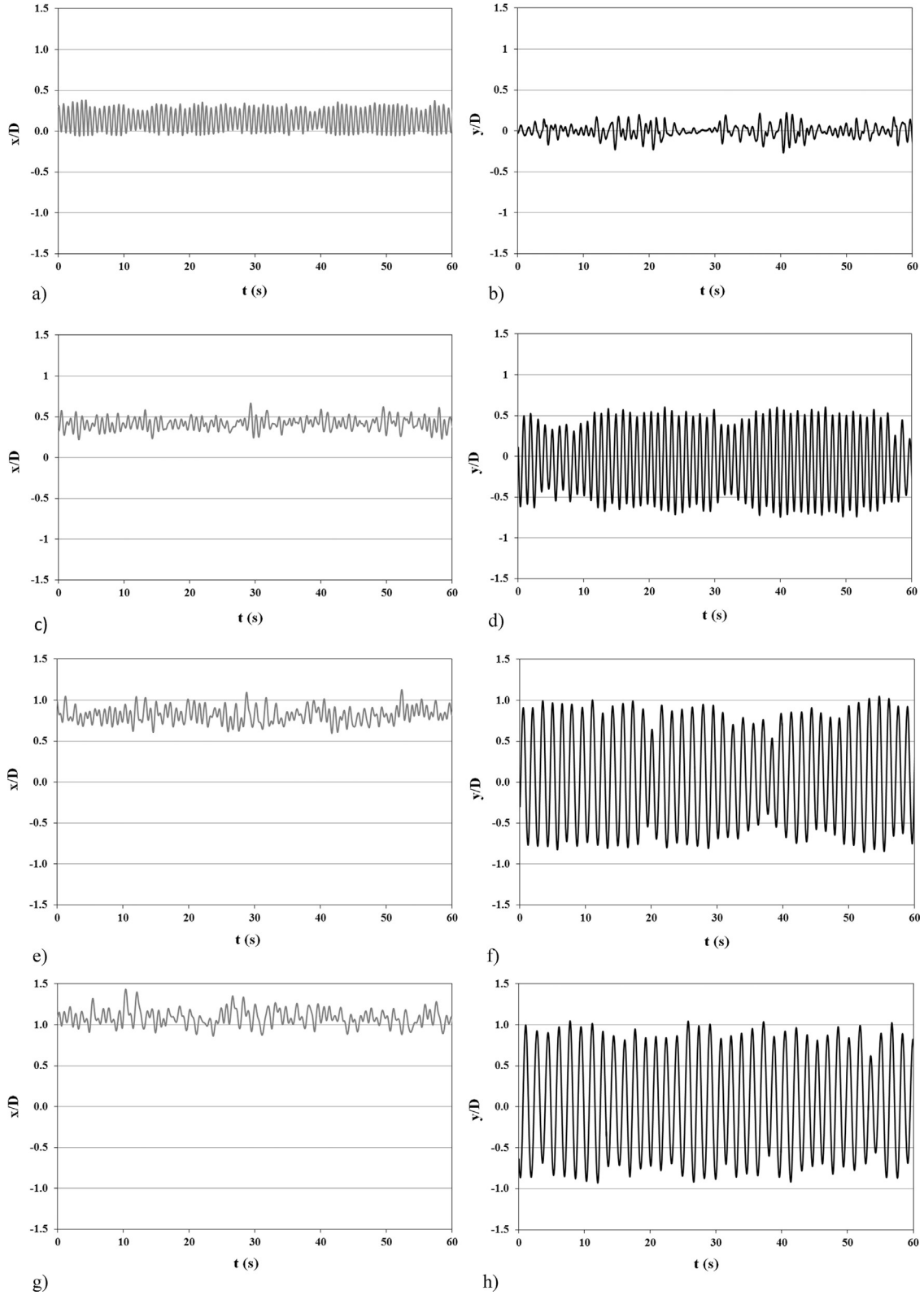


**Fig. 6.** Time histories of the non-dimensional vibration amplitudes, both in the streamwise and transverse directions: a), b) $U^* = 4.3$; c), d) $U^* = 5.9$; e), f) $U^* = 8.5$; g), h) $U^* = 10.5$.

are more chaotic than the counter clockwise ones, as also found by [18]. An explanation given in [18] for cylinder VIV is that, in counter clockwise trajectories, the body goes downstream after the vortices are shed, keeping closer to them as they go downstream too, and hence exploiting more the suction force. The timing of vorticity and body position for Mode I (clockwise trajectory) and II (counter clockwise trajectory) of the sphere VIV are reported in [5].

The $A^*_{x1}/A^*_{x2}$ ratio (Fig. 7b) is about 3 in $U^* \approx 5$, and then decreases as $U^*$ increases. In $U^* \approx 8$, $A^*_{x1}/A^*_{x2}$ approaches unity and remains almost constant as $U^*$ further increases. The comparison with $\left(A^*_{x1}/A^*_{x2}\right)_{crit}$ suggests whether the trajectory is self-intersecting (8-shape or crescent) or not ("egg", "rain-drop" or "D"). Only for $U^* = 5.1$, 5.5, and 9.6 - 11.6, $A^*_{x1}/A^*_{x2} > \left(A^*_{x1}/A^*_{x2}\right)_{crit}$ and thus the tra-

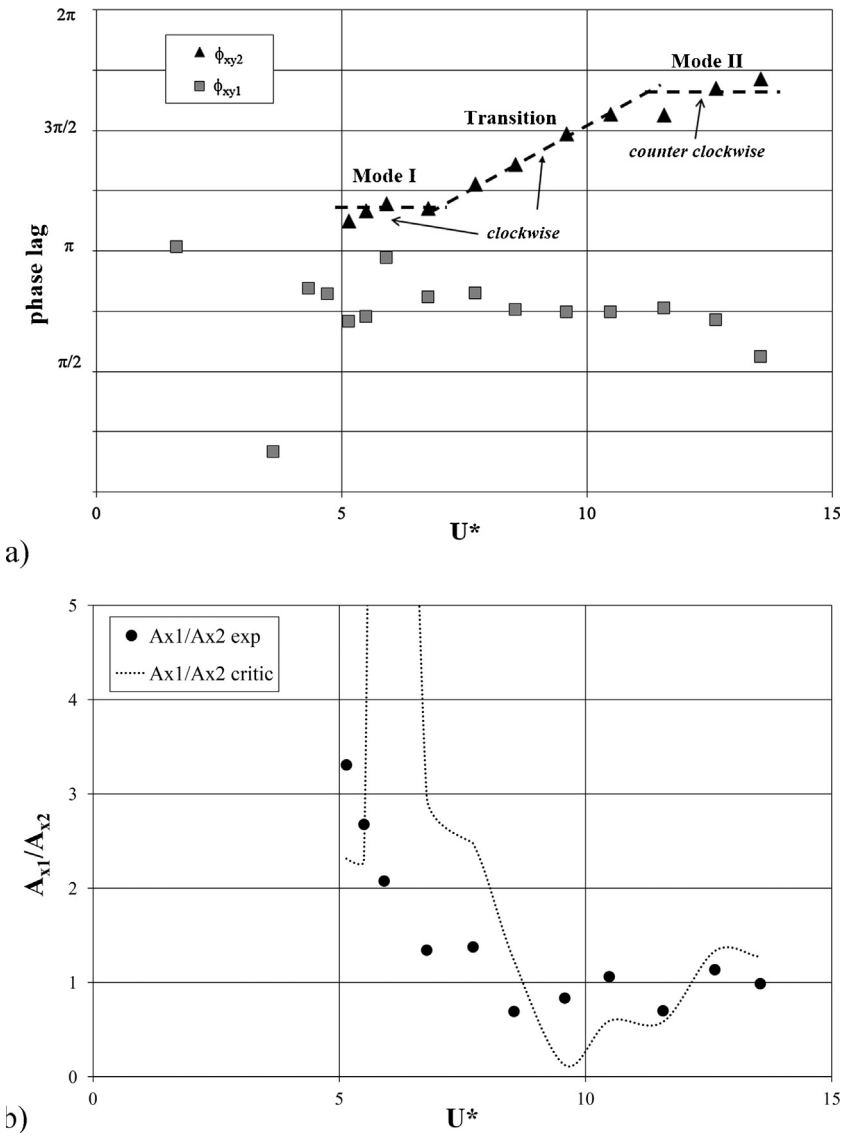


**Fig. 7.** a) Phase lag between streamwise and transverse motion. b) Ratio between the amplitudes of the streamwise motion.

jectory is not self-intersecting. This is visible in Fig. 8b, e and f, where the trajectories at $U^* = 5.1$, 9.6, and 10.5 are represented.

The self-intersecting trajectories have clockwise rotation (according to the definition of [18]) for $U^* < 10$ (Mode I and transition) and counter clockwise rotation for $U^* > 10$ (Mode II).

The trajectories depicted in Fig. 8 are a compendium of the trajectories encountered in this work. For $U^* = 5.1$, the trajectory almost has a "rain-drop" shape, though the value of $A^*_{x1}/A^*_{x2}$ is still larger than the critical value (the trajectory does not yet show a cusp). For $U^* = 5.9$, the trajectory is similar to the classical 8-shape, while for $U^* = 8.6$ it is still self-intersecting, but a lobe (the one in $y > 0$) is much smaller than the other. An increase of $U^*$ causes the trajectory to open up and to be not self-intersecting: for $U^* = 9.6$ the trajectory has a "D"- shape and for $U^* = 10.5$ it is halfway between the "D"-shape and "rain-drop" shape, and the tip of the trajectory is now in the region $y < 0$. The further increase of $U^*$ causes the trajectory to become self-intersecting again, with the smallest lobe in $y < 0$ ($U^* = 13.5$).

By looking at Fig. 8, it is evident that the phase-averaged trajectories and their inverse Fourier transforms are very close: this is a reliability proof of the analytical model of the trajectories (see the appendix for more details). Nevertheless, the raw experimental trajectory is often very noisy and its connection with its phase-average is hardly visible to the naked eye. This is due to the fact that, in the non-periodic motion component (either $x$ or $y$), the contribution of the main frequency $\omega$ (and its double $2\omega$) is often smaller than the contribution of other frequencies, which are not synchronised with the main frequency $\omega$, and hence do not contribute to characterise the periodic pattern of the trajectories. In order to quantify the amount of "periodicity" contained in the $x$ and $y$ components of motion, the subsequent indexes are calculated:

$$x_{periodicity} = \frac{\sqrt{A_{x1}^2 + A_{x2}^2}}{\sqrt{2}\sigma_x} \tag{8}$$

$$y_{periodicity} = \frac{A_y}{\sqrt{2}\sigma_y} \tag{9}$$

These indexes compare the amplitude calculated through the Fourier transform of the phase-averaged signal with the amplitude that the signal should have if it were perfectly periodic. In Fig. 9, the periodicity indexes are reported. It is possible to note that, for $U^* < 5$ the streamwise component is highly periodic and the transverse periodicity is very low (which indicates that the amplitudes of the other transverse motion frequencies are much higher than the amplitude of the oscillation frequency), decreasing as $U^*$ approaches 5. For $U^* > 5$, the $x$-periodicity increases with $U^*$ and

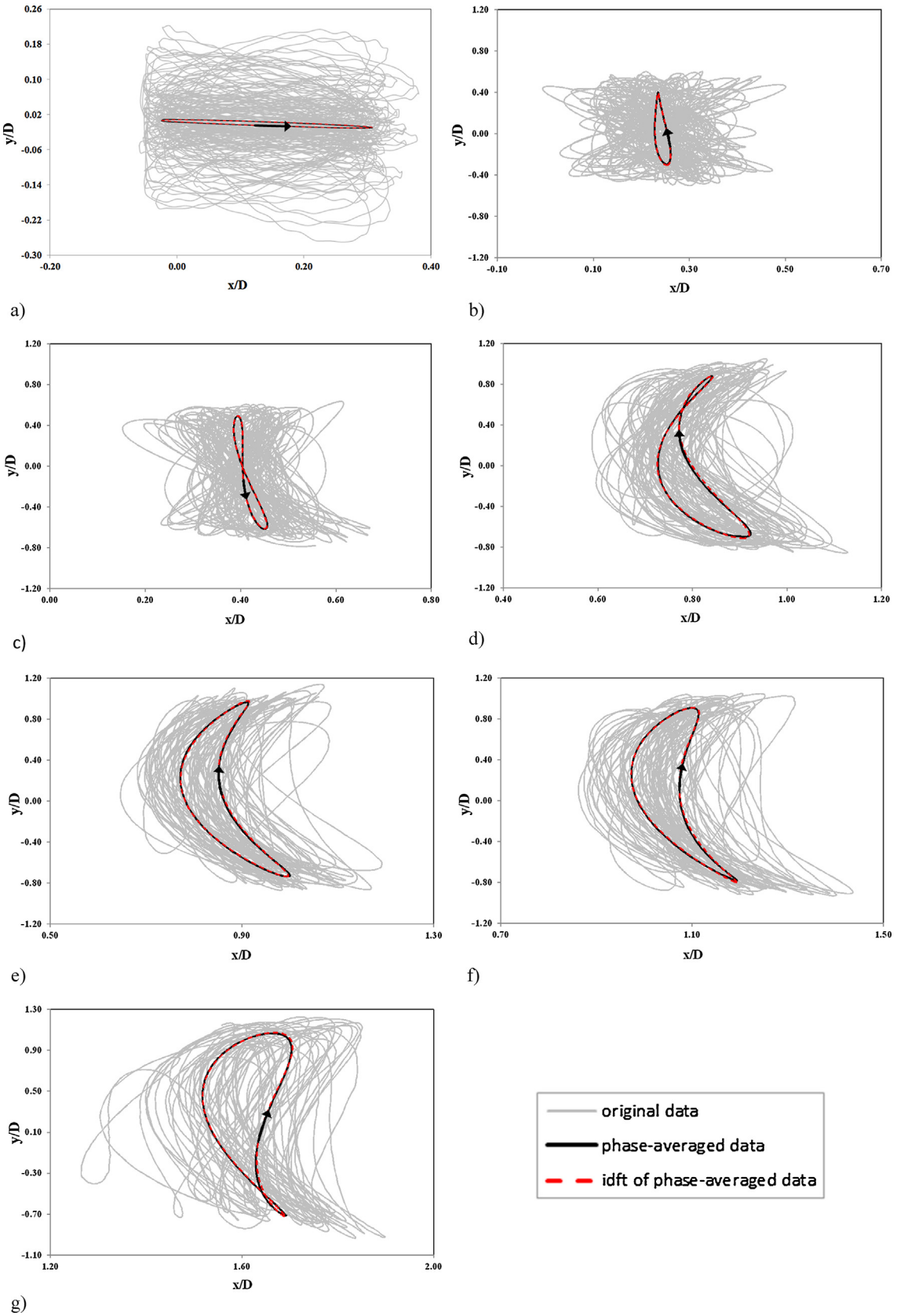


**Fig. 8.** Experimental raw trajectories with phase-averaged trajectories and inverse Fourier transform of phase-averaged trajectories superimposed. a) $U^*=4.3$; b) 5.1; c)$U^*=5.9$; d) $U^*=8.5$; e) $U^*=9.6$; f) $U^*=10.5$; g) $U^*=13.6$.

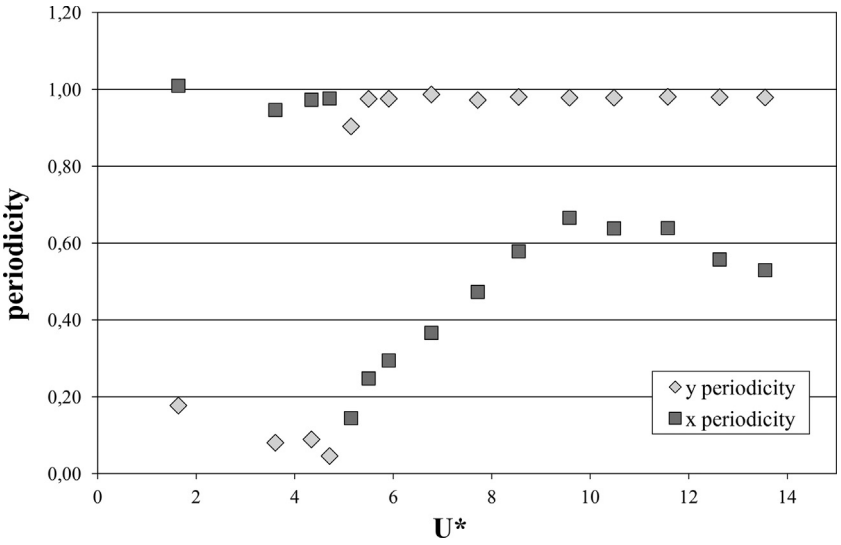


**Fig. 9.** "Periodicity" of streamwise and transverse motion.

reaches its maximum value of 0.6 in Mode II, higher than in Mode I, while the y-periodicity is high.

This different periodicity between the streamwise and transverse oscillations could be explained connecting $U^* \approx 5$ to the threshold value which divides the dynamic response in two synchronisation regions: a first region for $U^* < 5$, where the vortex shedding synchronises with the streamwise oscillations (Fig. 6a, b), and a second one for $U^* \geq 5$, where the vortex shedding synchronises with the transverse oscillations (Fig. 6c–h). In fact, theoretical and experimental results obtained by previous literature works on VIV spheres and cylinders [5–7,23,24] demonstrated the following: for low values of reduced velocity, the body motion is mainly excited by the fluctuating drag force associated with the vortex shedding; for high values of $U^*$, instead, and in particular since the resonance condition occurs (when the frequency of vibration is equal to the natural frequency), the motion begins to be mainly excited by the fluctuating lift force associated with the vortex shedding. Therefore, the oscillations happen as a consequence of the periodic forces applied to the sphere due to vortex shedding.

In particular, in the first region different authors [6,7] observed a periodic sequence of counter-rotating vortex pairs in the wake of the vibrating sphere. This sequence is similar to the vertical structures shedding visualised for a stationary sphere [25]. The sphere is then stimulated by periodic drag forces, which lead to a periodic motion in the line direction (Fig. 6a). The lift forces in this region are negligible and the transverse oscillations, being very low, are confused with the noise from external perturbations (Fig. 6b).

In the second region, instead, the formation of a chain of hairpin vortices in the plane normal to the flow, which shed periodically alternating on both sides of the sphere, puts the body through periodic lift forces [5,6,7]. This would justify the high periodicity of the transverse displacements (Fig. 6d, f, h). In this second region, there is no change in periodicity from Mode I to Mode II (Fig. 6f) because no different pattern of vortexes is observed but only a change in the timing of vortex formation, consistent with differences in the phase of the vortex force between the two modes [5].

The periodicity of the motion component, assumed as reference signal for the phase average ($x$ for $U^* < 5$ and $y$ for $U^* \geq 5$), is always close to the unity except for $U^* = 5.1$, where it is about 0.9. This indicates the switch from $x$-driven motion to $y$-driven motion.

In Figs. 10 and 11, the dimensionless frequency is reported respectively for streamwise and transverse components as a function of $U^*$. In both figures, the Power Spectral Density (PSD) of the motion component is represented by the inverted greyscale

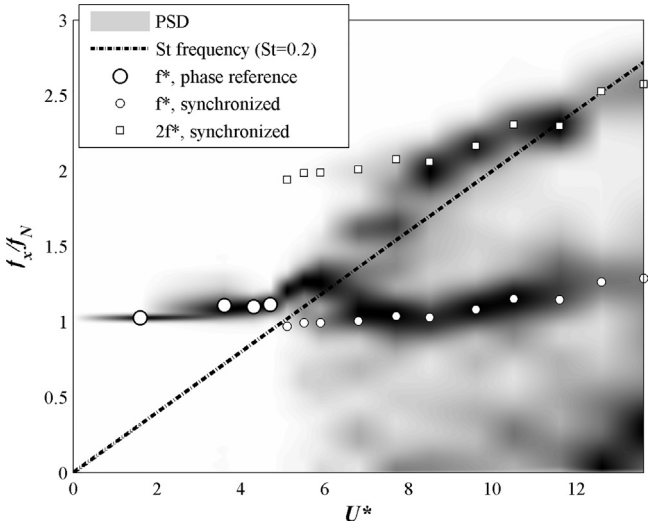


**Fig. 10.** Dimensionless frequency of streamwise motion.

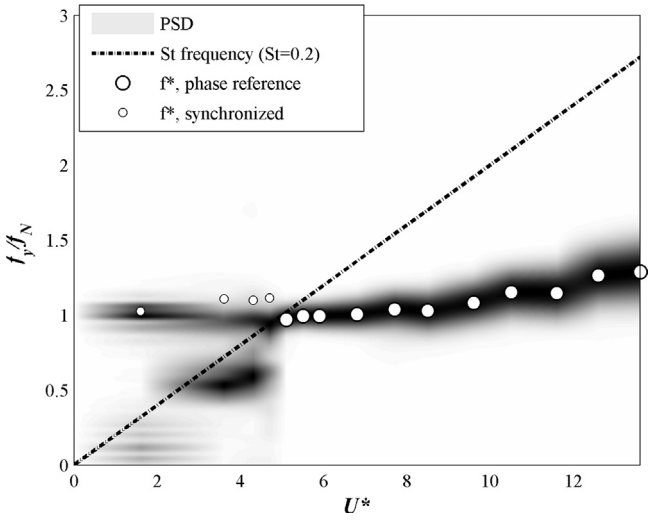


**Fig. 11.** Dimensionless frequency of transverse motion.

intensity (for each $U^*$, the PSD has been non-dimensionalised with respect to the maximum value found in the spectrum) and the Strouhal frequency for a fixed sphere is also reported, considering $St = 0.2$. The oscillation frequency $f^*$ is plotted as large circles if that motion component (either $x$ or $y$) is the phase reference (*i.e.* if it is the main motion component), otherwise as small circles (indicated as "synchronised"). In Fig. 10, the double of the oscillation frequency $2f^*$ is also plotted.

The value of the oscillation frequency $f^*$ agrees with literature results [5]: $f^*$ is close to the unity for $U^* < 5$; in $U^* = 5$ there is a small jump (decrement); and $f^*$ slowly increases with $U^*$, still remaining close to the unity.

Looking at the PSD map, a first observation is that the main motion component ($x$-component for $U^* < 5$ in Fig. 10 and $y$-component for $U^* \geq 5$ in Fig. 11) is characterised by a unique frequency peak, which coincides with the one calculated by phase average. On the contrary, the PSD of the secondary component (the non-periodic one) is scattered ($U^* \geq 5$ in Fig. 10 for the $x$-component and $U^* < 5$ in Fig. 11 for the $y$-component) and is distributed near the oscillation frequency, the double of the oscillation frequency, and/or the Strouhal frequency. In the secondary motion component (the non-periodic one), it must be noted that the oscillation frequency (or its double) is not always the dominant frequency of the spectrum. For example, in Fig. 10 for $U^* = 5$ - 6 very little power is associated to $f^*$ and $2f^*$; on the contrary, for $U^* > 8$ the PSD of the $x$-component concentrates in $f^*$ and $2f^*$. This agrees with the increase of $x$-periodicity shown in Fig. 9 and corresponds to the establishing of Mode II.

In the $x$-component, significant amount of power is also distributed in the low frequencies for $U^* > 8$, increasing with $U^*$.

## 5. Conclusion

In this paper, experimental investigations on an elastically mounted sphere with two linear degrees of freedom were performed under a wide range of reduced velocities ($1.6 \leq U^* \leq 13.6$). By analysing the dynamic response in amplitude and frequency and highlighting the comparative analysis of the motion trajectories, the following conclusions were reached:

1) the sphere showed a behaviour in amplitude and frequency similar to the tethered sphere, exhibiting Mode I (from $U^* \approx 5$ to $U^* \approx 8$), with oscillations between 0.4 and 0.65, and Mode II (from $U^* \approx 10$ to $U^* \approx 14$) characterised by higher amplitudes $0.8 \leq A_y^* \leq 1$. The "saturation amplitude" $A_y^* \approx 1$ at $U^* \approx 12$ was greater than the value 0.9 found by [5], probably due to the high Reynolds number. With regard to the dimensionless frequency, it was always close to unity, slightly increasing with $U^*$, in accordance with [5].
2) The PSD frequency analysis of the streamwise and transverse oscillations highlighted that the main motion component was characterised by a unique frequency peak, while the frequency content of the secondary component was more scattered and distributed near the oscillation frequency, its double, and/or the Strouhal frequency.
3) The discrete Fourier transform of the phase-averaged motion components revealed that the transverse motion was completely represented by one harmonic, while the streamwise motion was completely represented by a maximum of two harmonics of comparable magnitude.
4) For $U^* < 5$, the streamwise motion component was highly periodic and the transverse periodicity was very low. For $U^* > 5$, the crossflow motion component was highly periodic while the $x$-periodicity increased with $U^*$ and reached its maximum value in Mode II, higher than in Mode I.
5) Besides the classical 8-shaped trajectory, other trajectory shapes were detected. For $U^* < 5$, the trajectory was almost a segment. At the beginning of Mode I ($U^* \approx 5$), the trajectory had a "rain-drop" shape. When $U^* = 5.9$, the trajectory was similar to the classical 8-shaped one. As $U^*$ increased, the trajectory was distorted and one lobe of the 8 grew larger, until the trajectory opened up in a "D"-shape in Mode II at $U^* \approx 10$ - 12. A further increase caused the trajectory to become self-intersecting again, with the bigger lobe being on the opposite side of the 8.

## Acknowledgement

The authors would like to thank Dimitri Lefoulon, who realised the experimental tests during his MD thesis.

## Appendix A.

The trajectories were modelled considering one harmonic for the transverse component and a maximum of two harmonics for the streamwise component (one harmonic for $U^* < 5$). In Table A1, the Fourier coefficients (amplitudes) of the phase-averaged $x$ and $y$ motion are reported up to the fourth and third harmonic respectively for the $x$ and $y$ component. The coefficients are non-dimensionalised by the sphere diameter. The highlighted columns contain the coefficients used in the trajectory modelling; it can be seen that, for both the $x$ and $y$ components, the magnitude of the coefficients corresponding to higher harmonics is small compared to the ones considered for the model.

In Table A2, the coefficient of determination, $R^2$, calculated between the phase average and its inverse Fourier transform, is reported, for the $x$ and $y$ motion component. The highlighted columns indicate the $R^2$ between the phase-averaged $x$ and $y$ and the trajectory model, which indeed are where $R^2$ approximately reaches the unity.

**Table A1**
Amplitude of the Fourier coefficients of the phase-averaged $x$ and $y$ motion. The coefficients are dimensionless with respect to the sphere diameter. The highlighted columns contain the coefficients used in the modelling of the sphere motion.

| | $x$ | | | | $y$ | | |
|---|---|---|---|---|---|---|---|
| harmonic / $U^*$ | $\omega$ | $2\omega$ | $3\omega$ | $4\omega$ | $\omega$ | $2\omega$ | $3\omega$ |
| 1.6 | 0.065 | 0.001 | 0.001 | 0.001 | 0.001 | 0.000 | 0.000 |
| 3.6 | 0.125 | 0.003 | 0.000 | 0.000 | 0.006 | 0.000 | 0.000 |
| 4.3 | 0.166 | 0.003 | 0.001 | 0.000 | 0.009 | 0.001 | 0.000 |
| 4.7 | 0.172 | 0.001 | 0.000 | 0.000 | 0.004 | 0.000 | 0.000 |
| 5.1 | 0.015 | 0.005 | 0.000 | 0.000 | 0.351 | 0.004 | 0.001 |
| 5.5 | 0.023 | 0.009 | 0.000 | 0.000 | 0.485 | 0.003 | 0.002 |
| 5.9 | 0.028 | 0.014 | 0.001 | 0.000 | 0.552 | 0.000 | 0.001 |
| 6.8 | 0.033 | 0.024 | 0.002 | 0.001 | 0.623 | 0.003 | 0.004 |
| 7.7 | 0.044 | 0.032 | 0.001 | 0.000 | 0.654 | 0.003 | 0.005 |
| 8.5 | 0.045 | 0.065 | 0.003 | 0.002 | 0.798 | 0.006 | 0.010 |
| 9.6 | 0.058 | 0.069 | 0.001 | 0.002 | 0.858 | 0.005 | 0.010 |
| 10.5 | 0.065 | 0.061 | 0.001 | 0.001 | 0.854 | 0.006 | 0.010 |
| 11.6 | 0.054 | 0.078 | 0.004 | 0.002 | 0.983 | 0.016 | 0.013 |
| 12.6 | 0.069 | 0.061 | 0.003 | 0.002 | 0.884 | 0.009 | 0.011 |
| 13.6 | 0.057 | 0.058 | 0.002 | 0.002 | 0.897 | 0.002 | 0.011 |

**Table A2**
$R^2$ coefficient between the phase-average and its inverse Fourier transform up to the n-th harmonic. Columns highlighted indicate the $R^2$ coefficient between the phase-averaged trajectories and the trajectory model.

| | $x$ | | | | $y$ | | |
|---|---|---|---|---|---|---|---|
| harmonic / $U^*$ | $\omega$ | $2\omega$ | $3\omega$ | $4\omega$ | $\omega$ | $2\omega$ | $3\omega$ |
| 1.6 | 1.000 | 1.000 | 1.000 | 1.000 | 0.995 | 0.998 | 0.998 |
| 3.6 | 0.999 | 1.000 | 1.000 | 1.000 | 0.984 | 0.991 | 0.993 |
| 4.3 | 1.000 | 1.000 | 1.000 | 1.000 | 0.993 | 0.996 | 0.997 |
| 4.7 | 1.000 | 1.000 | 1.000 | 1.000 | 0.979 | 0.991 | 0.994 |
| 5.1 | 0.913 | 0.997 | 0.998 | 0.998 | 1.000 | 1.000 | 1.000 |
| 5.5 | 0.877 | 1.000 | 1.000 | 1.000 | 1.000 | 1.000 | 1.000 |
| 5.9 | 0.811 | 0.999 | 1.000 | 1.000 | 1.000 | 1.000 | 1.000 |
| 6.8 | 0.654 | 1.000 | 1.000 | 1.000 | 1.000 | 1.000 | 1.000 |
| 7.7 | 0.654 | 1.000 | 1.000 | 1.000 | 1.000 | 1.000 | 1.000 |
| 8.5 | 0.323 | 0.998 | 0.999 | 1.000 | 1.000 | 1.000 | 1.000 |
| 9.6 | 0.410 | 0.999 | 0.999 | 1.000 | 1.000 | 1.000 | 1.000 |
| 10.5 | 0.529 | 1.000 | 1.000 | 1.000 | 1.000 | 1.000 | 1.000 |
| 11.6 | 0.327 | 0.998 | 1.000 | 1.000 | 1.000 | 1.000 | 1.000 |
| 12.6 | 0.562 | 0.998 | 0.999 | 1.000 | 1.000 | 1.000 | 1.000 |
| 13.6 | 0.493 | 0.999 | 0.999 | 1.000 | 1.000 | 1.000 | 1.000 |

## References


[1] Vortex Hydro Energy, 2013, http://www.vortexhydroenergy.com/ (Accessed 01 April 2013).
[2] E. Naudascher, D. Rockwell, Flow Induced Vibration: An Engineering Guide, Balkema, Rotterdam, 1993.
[3] C.H.K. Williamson, R. Govardhan, Dynamics and forcing of a tethered sphere in a fluid flow, J. Fluids Struct. 11 (1997) 293–305.
[4] N. Jauvtis, R. Govardhan, C.H.K. Williamson, Multiple modes of vortex-induced vibration of a sphere, J. Fluid Struct. 15 (2001) 555–563.
[5] R.N. Govardhan, C.H.K. Williamson, Vortex-induced vibrations of a sphere, J. Fluid Mech. 531 (2005) 11–47.
[6] R. van Hout, A. Krakovich, O. Gottlieb, Time resolved measurements of vortex-induced vibrations of a tethered sphere in uniform flow, Phys. Fluids 22 (2010), 087101-1-087101-11.
[7] R. van Hout, A. Katz, D. Greenblatt, Acoustic control of vortex-induced vibrations of a tethered sphere, AIAA J. 51 (754) (2013), Technical Notes.
[8] H. Lee, K. Hourigan, M.C. Thompson, Vortex-induced vibration of a neutrally buoyant tethered sphere, J. Fluid Mech. 719 (2013) 97–128.
[9] S. Behara, I. Borazjani, F. Sotiropoulos, Vortex-induced vibration of an elastically mounted sphere with three degrees of freedom at Re = 300; hysteresis and vortex shedding modes, J. Fluid Mech. 686 (2011) 426–450.
[10] S. Behara, F. Sotiropoulos, Vortex-induced vibrations of an elastically mounted sphere: the effects of Reynolds number and reduced velocity, J. Fluids Struct. 66 (2016) 54–68.
[11] D. Mirauda, S. Malavasi, A. Volpe Plantamura, Analysis of effects of the free surface on the movement of a tethered sphere immersed in a steady flow, in: 9th International Conference on Flow-induced Vibrations, FIV 2008, Praga, 2008, pp. 835–840.
[12] D. Mirauda, A. Volpe Plantamura, S. Malavasi, Hydrodynamic forces acting on an oscillating structure, WIT Trans. Ecol. Environ. 149 (2011) 321–331, WIT Press.

[13] D. Mirauda, A. Volpe Plantamura, S. Malavasi, Boundaries effects on the movements of a sphere immersed in a free surface flow, J. Offshore Mech. Arct. Eng. 133 (2011), 041301-1-041301-5.
[14] D. Mirauda, A. Volpe Plantamura, S. Malavasi, Boundaries influence on the flow field around an oscillating sphere, Proceedings of the ASME 2013 32nd International Conference on Ocean, Offshore and Arctic Engineering OMAE2013 (2013).
[15] D. Mirauda, A. Volpe Plantamura, S. Malavasi, Dynamic response of a sphere immersed in a shallow water flow, J. Offshore Mech. Arctic Eng. 136 (2014), 021101-1-021101-6.
[16] A. Krakovich, L. Eshbal, R. van Hout, Vortex dynamics and associated fluid forcing in the near wake of a light and heavy tethered sphere in uniform flow, Exp. Fluids 54 (2013) 1615.
[17] M. Negri, F. Cozzi, S. Malavasi, Self-synchronized phase averaging of PIV measurements in the base region of a rectangular cylinder, Meccanica 46 (2) (2011) 423–435.
[18] J.M. Dahl, F.S. Hover, M.S. Triantafyllou, S. Dong, G.E. Karniadakis, Resonant vibrations of bluff bodies cause multivortex shedding and high frequency forces, Phys. Rev. Lett. 99 (2007), 144503-1-144503-4.
[19] R. Bourguet, G.E. Karniadakis, M. Triantafyllou, Vortex-induced vibrations of a long flexible cylinder in shear flow, J. Fluid Mech. 677 (2011) 282–342.
[20] Z. Kang, L. Jia, An experimental study of a cylinder's two degree of freedom VIV trajectories, Ocean Eng. 70 (2013) 129–140.
[21] Z. Kang, N.I. Wenchi, L. Sun, An Experimental investigation of two-degrees-of-freedom VIV trajectories of a cylinder at different scales and natural frequency ratios, Ocean Eng. 126 (2016) 187–202.
[22] R.N. Govardhan, C.H.K. Williamson, Defining the 'modified Griffin plot' in vortex-induced vibration: revealing the effect of Reynolds number using controlled damping, J. Fluid Mech. 561 (2006) 147–180.
[23] S.S. Chen, J.A. Jendrzejczyk, Dynamic response of a circular cylinder subjected to liquid cross flow, Trans. ASME 101 (1979) 106–112.
[24] T. Sarpkaya, A critical review of the intrinsic nature of vortex-induced vibrations, J. Fluids Struct. 19 (2004) 389–447.
[25] H. Sakamoto, H. Haniu, A study on vortex shedding from spheres in a uniform flow, J. Fluids Eng. 112 (1990) 386.